Corrosion Science 215 (2023) 111056

Contents lists available at ScienceDirect

Corrosion Science

journal homepage: www.elsevier.com/locate/corsci

Evolution of surface film in AA2024-T3 after a long-term immersion in NaCl solution

J. Christudasjustus *, V.B. Vukkum, R.K. Gupta *

Department of Materials Science and Engineering, North Carolina State University, Raleigh, NC 27606, United States of America

ARTICLE INFO

Keywords:
AA2024
Cu clusters
Corrosion product
Pitting corrosion
Aluminum alloys

ABSTRACT

Surface films of AA2024-T3 after immersion in 0.1 M NaCl for 14 days, 6 months, and 1 year have been investigated using scanning electron microscopy. The corrosion product generated on the surface over the immersion period was comprised of porous outer and compact inner layers. The Cu enrichment at the corrosion product/metal interface and Cu clusters within the surface films have been observed. Exfoliation corrosion was observed, which allows the electrolyte to migrate through exfoliated path and cause rapid corrosion at subsurface level. Mechanistic aspects of surface film, Cu cluster formation, and corrosion under the surface film have been discussed.

1. Introduction

AA2024-T3 is a legacy Al alloy that has been extensively used in aircraft manufacturing for decades [1–3]. The T3 temper condition (i.e., solution heat treated → cold worked → naturally aged) causes fine precipitates that are desirable for strength but renders alloy prone to localized corrosion [4,5]. Al-Cu-Mg type (S phase) and Al_2Cu (θ phase) are the main strengthening precipitates. Additionally, undesirable coarse intermetallic particles (IPs) known as constituent particles are also present. Al_7Cu_2Fe, Al_6MnFe_2, $(Al,Cu)_6Mn$, and $Al_{20}Cu_2(MnFe)_3$ are the most common and abundant constituent particles [6–8]. The IPs induce localized corrosion in the form of pitting and intergranular attack, generating a potential site for cracking [9]. While most common IPs in AA2024-T3 are classified as cathodic, the S-phase exhibit dual behavior, which is anodic in the beginning and changes to cathodic after the preferential dissolution of Al and Mg [10]. The cathodic IPs promote oxygen reduction reaction, which causes an alkaline environment around its immediate vicinity [11,12]. As the pH increases in that region, the protective oxide of Al becomes unstable and alkaline dissolution of the alloy begins [13]. Understanding and quantifying the pitting corrosion in Al alloys become complex due to the large variation in composition, size, morphology, and spatial distribution of IPs.

Surface characterization after corrosion tests has been reported to understand the localized corrosion mechanisms and role of various microstructural features. Literature has widely reported the remnants of Cu clusters within the corroded region in AA2024-T3 alloy [14–18]. The Cu clusters originate from two sources - IPs and solid solution. Cu clusters occurring from IPs involve the preferential dissolution of IPs, where more active elements such as Al, Mn and Fe are selectively dissolved, and the sponge-like local Cu clusters are left behind [5]. These Cu clusters are either captured by the hydrous corrosion product and move away due to mechanical transport as the film grows or get redistributed over the surface to promote further secondary pitting corrosion [16]. Also, the Cu clusters can dissolve themselves with time if they are electrochemically isolated from the matrix [16]. Meanwhile, Cu from solid solution and nano-sized precipitates emerge from the selective dissolution of Al followed by surface diffusion that results in uniform enrichment of nano-sized Cu layer at corrosion product/metal interface [13,19,20]. The local clusters and enrichment phenomena of Cu have been investigated using electrochemical techniques (such as rotating disk electrode, rotating ring-disk electrode, three-electrode cell) and characterization tools (e.g., electron microscopy, atomic force microscopy, scanning kelvin probe force microscopy). However, the long-term immersion generates huge corrosion product on the surface that becomes difficult to investigate the pit initiation and morphology buried beneath it. Removing the corrosion product could lose the surface details, for instance, the position of Cu clusters within the pit and surface, progressive dissolution of IPs, and morphology of the corrosion product at the interface. Therefore, one of the objectives of this study is to reveal the Cu clusters with the corrosion product intact up to 1-year immersion.

The top surface analysis approach often provided a partial picture and lacked detail from the sub-surface of the materials buried beneath.

* Corresponding authors.
E-mail addresses: jchris22@ncsu.edu (J. Christudasjustus), rkgupta2@ncsu.edu (R.K. Gupta).

https://doi.org/10.1016/j.corsci.2023.111056
Received 16 November 2022; Received in revised form 13 February 2023; Accepted 16 February 2023
Available online 17 February 2023

To overcome this obstacle, the focused ion beam (FIB) technique has been used to obtain the cross-section of the material surface, which helps to get a visual interpretation of the fundamental mechanism of gradual pitting, intergranular attack, and exfoliation corrosion. For instance, studying the clustering of the IPs forming a network at the sub-surface during the corrosion process [21,22], examining the surface at an angle to reveal the dealloying of S-phase (Al_2CuMg) particles, matrix/-particle interfacial attack, and grain boundary attack. However, characterization through FIB becomes challenging when the region of interest is hundreds of microns deep and wide, which requires a large area of investigation. For instance, immersion for up to 6 months in 0.1 M NaCl generates pits of hundreds of microns and a thick hydroxide layer through uniform corrosion and pitting [23,24]. Cross-sectional analysis of such surface is not evidently reported due to the difficulty in characterizing the huge portion of corrosion product. It is of scientific interest to explore the surface phenomena after long-term immersion, and new ways of investigation often provide additional insight into the corrosion mechanisms. Moreover, the literature reports the corrosion properties and fundamental mechanisms investigated in 0.1 M NaCl for many advanced engineering aluminum alloys as it facilitates observing the slow thermodynamics and corrosion kinetics occurring at the surface [25–31]. Such studies require a reference of corrosion behavior occurring in commercial Al alloys, where the corrosion kinetics are comparable and easier to study compared to the high concentration of chloride solution counterpart. Thus, signifying the importance of the electrolyte used in this study.

The present study demonstrates an approach to visually reveal the wide range of cross-sectional morphology after exposure to different immersion periods (14 days, 6 months, and 1 year) in 0.1 M NaCl environment. This method can collect information in the order of millimeters, particularly when the region of interest is much larger. Because of the large analyzing region, it offers various evidence at single-time specimen preparation without much effort. The work addresses the morphology and growth of corrosion products formed after various immersion periods, the role of IPs in influencing surface exfoliation, and the dissolution of Al-Cu-Fe-Mn particles. The findings reveal the substantial influence of sub-surface activity in promoting the acceleration or sustainability of corrosion events on the surface.

2. Experimental procedure

2.1. Material and immersion process

The chemical composition of AA2024-T3 alloy plate used in the present study is provided in Table 1. The 3 mm thick AA2024-T3 plate was cut into 20 × 10 mm coupons. They were ground to 800 and 1200 grit SiC paper under tap water and subsequently polished to 3 and 0.05 μm surface finish using polycrystalline diamond suspension. After that, specimens were ultrasonicated for 5 min in ethanol to remove contamination.

The immersion was performed in 0.1 M NaCl as widely used in literature [23,32]. The polished specimens were immersed in the beaker with 250 mL of 0.1 M NaCl solution. The beaker was covered with parafilm with some holes, and the specimens were left undisturbed for 14 days, 6 months, and 1 year at room temperature (~22 ℃). During the immersion period, deionized water was added at a regular interval of two weeks to compensate for the water evaporating from the electrolyte. After the specified immersion period, the specimens were removed, and plenty of deionized water was poured on the specimens to remove the NaCl residue.

2.2. Characterization

Scanning electron microscopy (SEM) was performed on the top surface of a 1-year immersed specimen to obtain the elemental distribution within the corrosion product. The electron was incident at 15 kV with 0.8 nA current. X-ray photoelectron spectroscopy (XPS) was performed on the top surface to understand the chemical composition with respect to the binding energy. The analyzing chamber pressure of XPS was maintained below 10^{-9} mbar, and Mg anode was used as the X-Ray source of 300 W. The experiment was performed with the take-off angle of 60° over the 2 × 2 mm area. Initially, the surface was sputtered for a few nanometers to remove the residue coming from carbon contamination. The survey scan was taken from 0 to 1100 eV to observe the elements present in the corrosion product. Thereafter, the high-resolution core-level spectra of detected O 1s, Al 2p and Fe $2p_{3/2}$ were recorded. The analysis of XPS was conducted using CASA software that provides the relative sensitivity factor given by Scofield [33] and the background was subtracted using the Shirley function.

Grazing incidence X-ray diffraction (GIXRD) was performed on the top surface of 14-day and 1-year immersed specimens to obtain the chemical composition of the corrosion product. Cu Kα radiation with the incidence angle of 0.5° was used to acquire the information from the 2θ range of 15°–85°, having a scan rate of 1°/min and 0.01° step size.

To investigate the cross-sectional region of specimens after the immersion for different periods, all six sides of the specimen surface were electroplated with copper. The electroplating is to protect it from being damaged during epoxy mounting and polishing. Cu electroplating was performed at ~2 V, having the current density around 9 mA/cm^2 for 10 min, simultaneously confirming that the Cu was visibly deposited. Later, the specimens were mounted in epoxy with the transverse side exposed from the top, as shown in Fig. 1, followed by 0.05-micron polishing to carefully expose the fresh surface for analyzing the cross-sectional morphology. These cross-sectional surfaces were studied using a scanning electron microscope (SEM) at 20 kV with 0.8 nA current. Energy-dispersive X-ray spectroscopy (EDS) was performed to confirm the elemental distribution and intermetallic particles (IPs).

3. Results

The backscattered electron (BSE) image presented in Fig. 2 shows the microstructure of AA2024-T3 with various intermetallic particles (IPs)

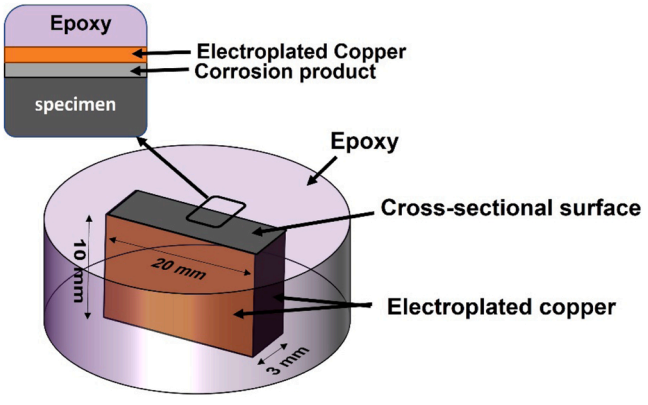

Fig. 1. Schematic representation of the AA2024-T3 specimen prepared for cross-sectional analysis.

Table 1
Chemical composition of AA2024-T3 in wt%.

Alloy	Cu	Mg	Mn	Fe	Zn	Si	Ti	V	Cr	Al
2024-T3	4.4	1.4	0.53	0.20	0.10	0.08	0.02	0.01	0.01	Bal.

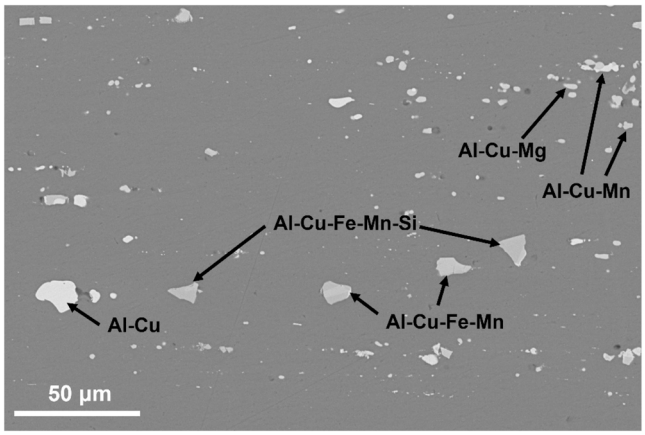

Fig. 2. Backscattered electron image showing the microstructure of AA2024-T3 with intermetallic particles.

identified by EDS analysis. The elemental composition of IPs were Al-Cu, Al-Cu-Fe-Mn, Al-Cu-Fe-Mn-Si, Al-Cu-Mg, and Al-Cu-Mn, which is consistent with the literature [1,6,8]. The sizes of Al-Cu, Al-Cu-Fe-Mn, and Al-Cu-Fe-Mn-Si were larger than 5 µm while Al-Cu-Mg and Al-Cu-Mn were smaller in size of < 5 µm.

3.1. AA2024-T3 after 14-days immersion

The surface morphology of the AA2024-T3 specimen from a cross-sectional view after 14 days of immersion is shown in Fig. 3. The dark contrast over the surface shows a thick layer of corrosion product. The corrosion product layer formed after 14 days seems to be intact and adherent to the surface, exhibiting a thickness range of 8–10 µm with an average of 9.3 µm (Fig. 3), and therefore, it is termed an intact corrosion product layer hereafter. Several IPs were observed within the intact corrosion product, as shown by white arrows in Fig. 3a. Additionally, loose corrosion product with 10–11 µm thickness over the intact layer was observed in several places, for instance, above the Al-Cu-Fe-Mn particle, as shown in Fig. 3b. The cracks observed within the corrosion product are generally termed mud-cracking that is visible across the layer and form due to dehydration once removed from the electrolyte and exposed to the vacuum environment of SEM. Additionally, fine Cu particles can be observed enriching at the corrosion product/metal interface, which could be either in metallic or oxide form. The layer of Cu enrichment can possibly come from two sources: 1) the Cu present in solid solution and 2) the presence of nano-sized precipitates such as Al_2Cu (θ phase) and Al_2CuMg (S phase) [20]. AA2024-T3 alloy has 4.4 wt% Cu in which some are consumed in secondary phases such as constituent particles and precipitates, while the remaining are present in solid solution. During the corrosion, the electrochemically active metal will preferentially dissolve compared to noble metal. Al, being highly reactive, will have higher dissolution kinetics compared to Cu. Thus, Cu-enriched layer is formed at the corrosion product/metal interface. Moreover, the Cu enrichment phenomenon can also be explained from the Gibbs free energy, where the Gibbs free energy for forming Al oxide is lower than that for Cu oxide [34].

3.2. AA2024-T3 after 6-months immersion

After 6 months of immersion, the surface showed the generation of a large amount of porous loose corrosion product formed above the intact layer compared to 14 days of immersed surface, as shown in Fig. 4a. The thickness range of porous loose corrosion product was 40–62 µm, while the intact layer showed a slight increment in thickness range of 9–11 µm. Several pits are seen beneath the thick corrosion product layer over the matrix, as shown in Fig. 4a. These pits appear to be shallower, with more prolonged immersion leveling with the corrosion product/metal interface. Clusters of IPs are observed within the pit, indicating the source of the pit origin (Fig. 4a). Interestingly, apart from the Cu enrichment at the interface, an additional thin layer of Cu enrichment along the center of the intact corrosion layer indicates the fluctuation of dissolution kinetics as the corrosion progresses. Fig. 4b shows several fascinating events in a magnified view. Mildly etched grain boundaries can be observed beneath the pit vicinity, implying the progression of corrosion through the intergranular path promoting intergranular corrosion (IGC). The IGC could also be a combined result of exfoliation corrosion, a form of corrosion that tears apart the elongated grains near the surface in high-strength Al alloys [35]. A fissure initiating the exfoliation corrosion is observed to penetrate through the pit and propagate through grain boundaries, while some of their secondary paths appear to be diverging towards IPs. Fig. 5a presents a high-magnification BSE image demonstrating the exfoliation corrosion forming a network to reach adjacent IPs. As the exfoliation corrosion initiates and approach IPs, they were seen mostly traveling along the particle/matrix interface. These exfoliated regions can potentially channel the aggressive electrolyte and initiate the sub-surface corrosion of the matrix. The dark contrast regions enveloped along the exfoliated path shown by white arrows indicate the dissolution of the matrix as the electrolyte has penetrated and initiated the hydrolysis. The formation of corrosion product within this region could weaken the grain boundaries

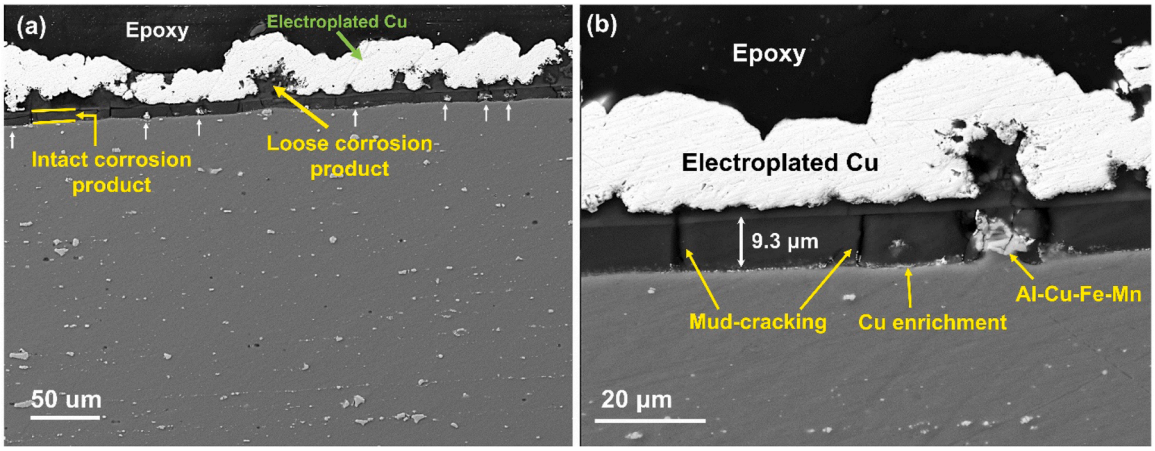

Fig. 3. (a) Low magnification cross-sectional view of AA2024-T3 after 14 days immersion in 0.1 M NaCl. The white arrows show the intermetallic embedded within the layer while some are still attached with the matrix. (b) High magnification image showing intact corrosion product layer thickness of ~9.3 µm and a representative example of intermetallic embedded within the layer.

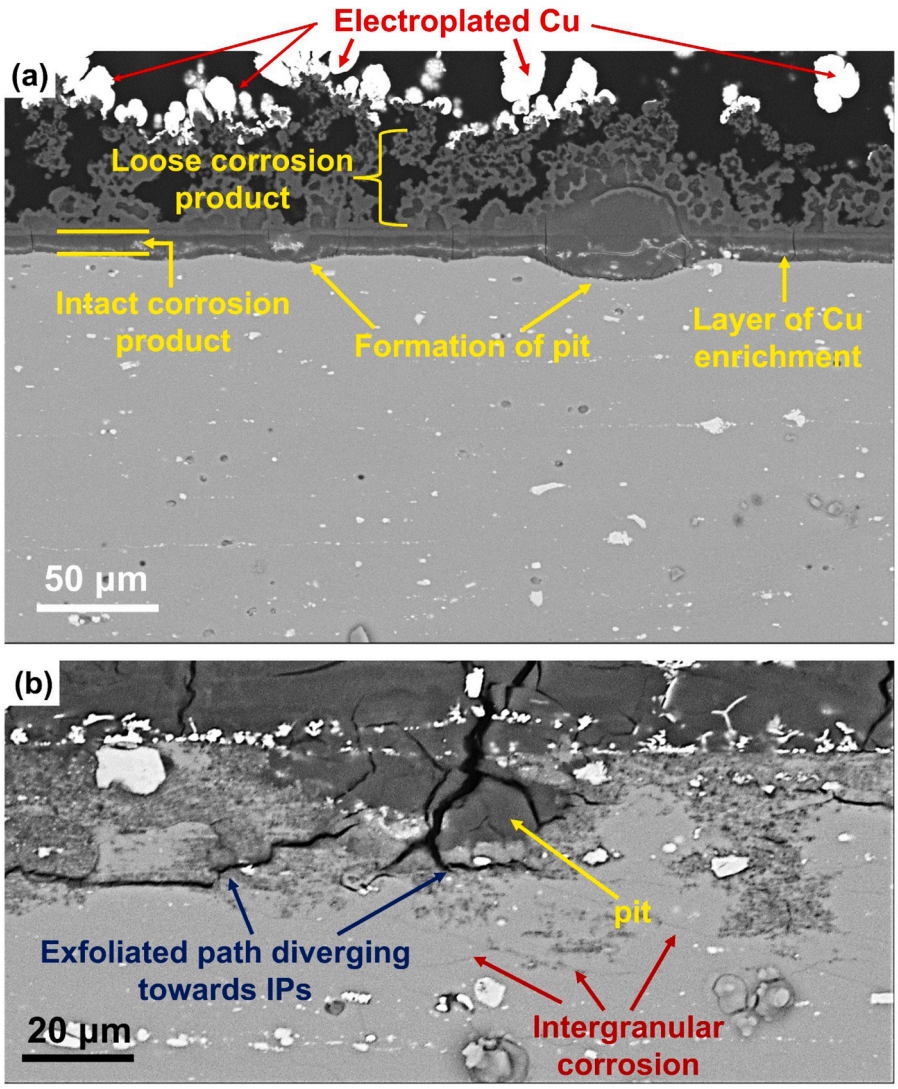

Fig. 4. (a) Low magnification cross-sectional view of AA2024-T3 after 6 months immersion in 0.1 M NaCl, and (b) High magnification BSE image showing intergranular corrosion beneath the pit and exfoliated path moving through grain boundaries and diverging towards IPs.

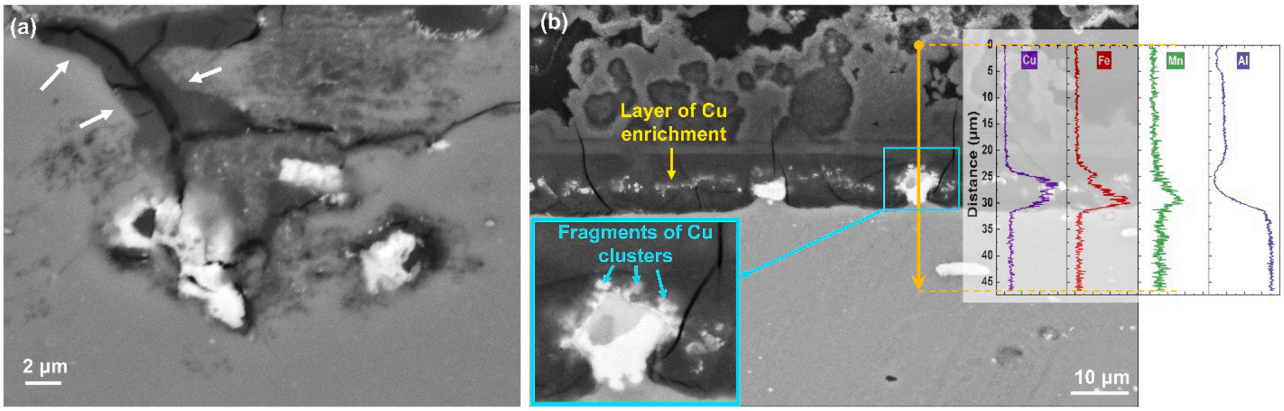

Fig. 5. (a) High magnification image shows the exfoliated path along intermetallic particles. The white arrows indicate the penetration of electrolyte and dissolution of matrix along the rupture. (b) Thin layer of Cu enrichment observed within the intact corrosion product layer, and the EDS line-scan reveals the progressive dissolution of Al-Cu-Fe-Mn intermetallic. The inset image shows the fragments of Cu clusters collapsing from the particle.

resulting in detachment of surface grains along with the progressive intergranular attack weakening the intergranular bond.

A clear view of Cu enrichment within the intact layer and a good example of the partial dealloying of the Al-Cu-Fe-Mn particle is shown in Fig. 5b. The EDS line-scan analysis was performed on that particle to reveal elemental distribution. The partially dissolved upper half of the

Al-Cu-Fe-Mn particle exhibited no sign of Al, a negligible amount of Mn, a low amount of Fe, and the same amount of Cu compared to the bottom half. The zoomed-inset image reveals the progressive breaking of the Al-Cu-Fe-Mn particle, where the top periphery showed fragments of Cu detaching from the particle. Among these detached Cu clusters, some exhibit solid-like pieces while others seem to be expanding and depicting sponge-like characteristics. The sponge-like structure of Cu was also reported for S-phase by Buchheit et al. [5] and Vukmirovic et al. [13].

3.3. AA2024-T3 after 1-year immersion

The surface of the long-term immersion specimen for up to 1 year formed a massive corrosion product, as shown in Fig. 6a. The thickness range of the loose corrosion product layer showed 71–90 μm, while the intact corrosion product layer exhibited a thickness range of 12–15 μm. The loose corrosion product layer internally displayed gradual structural differences where the outermost part exhibited a spongy (porous) region, and the inner part near the alloy surface showed a dense structure, comparatively (Fig. 6b). A possible explanation could be the transition of oxide to hydroxide species. The region near the alloy surface could be rich in oxide form, which is initially formed due to lower formation energy than hydroxide [36,37]. In comparison, the outermost region could be rich in hydroxide species. As the transition of oxide to hydroxide takes place, the structure expands to reduce the surface energy. Additionally, the outermost part of the corrosion product continuously interacts with the electrolyte; therefore, the region experiences expedited dissolution compared to the inner region. The interface between intact and loose corrosion products began to display a flawed and debonding feature, unlike in 6 months specimen where a clean adherence was visible. Several large pits were captured, as seen in Fig. 6c and 6d. A high density of local sponge-like Cu clusters could be seen within these pits. Within the sponge-like Cu clusters, some Cu fragments still show a solid-like structure, which could be either in metallic or oxide form. The local accumulation of Cu clusters seems to be generated by IPs, while the Cu enrichment layer across the corrosion product/metal interface could be easily differentiated to be coming from solid solution decomposition. The pit vicinity showed etched grain boundaries indicating the IGC activity, while this behavior was not observed beneath the uniform corrosion surface. The top view of the corrosion product formed after 1-year immersion, along with the EDS mapping, is shown in Fig. 7. The surface was observed to be charging due to the obstruction of electron flow by corrosion product that generally promotes poor conductivity. A substantial presence of Cl was detected over the corrosion product. The elemental distribution from the alloy composition showed the strong presence of Al and O with lower content of Mg, Cu, Si, Mn, and Fe.

X-ray photoelectron spectroscopy (XPS) was performed over the corrosion product to obtain the chemical composition through binding energies, as shown in Fig. 8. Table 2 provides the binding energy (BE), full widths at half maximum (FWHM), and intensities of the deconvoluted peaks from high-resolution core-level spectra. The survey scan detected the signals from O, Al, and Fe (Fig. 8a). The high-resolution O 1s peak was fitted with two components – O $1s_A$ and O $1s_B$ (Fig. 8b). The O $1s_A$ peak at lower binding energy (530.9 eV) corresponds to the oxide contribution from Al and Fe, while the O $1s_B$ peak (531.7 eV) is attributed to the hydroxyl group (likely $Al(OH)_3$ and FeO(OH) species). The Al 2p core-level peak in Fig. 8c was fitted with three deconvoluted peaks. The higher BE (75.4 eV) is assigned to Al(III) ions showing the contribution from $Al(OH)_3$, the lower BE (74.2 eV) is assigned to Al(III) ions exhibiting Al_2O_3, and the lowest BE (72.8 eV) is assigned to metallic Al. The small contribution from Fe $2p_{3/2}$ core-level peak is deconvoluted using multiplet splitting mentioned by Grosvenor et al. and Biesinger et al. [38,39]. The multiplet splitting peaks of FeO represent the Fe^{2+} species having oxide contribution and appeared at 708.4 eV, 709.6 eV, and 710.9 eV. The multiplet splitting peaks of FeO(OH) representing the Fe^{3+} species having hydroxide contribution appeared at 710.2 eV, 711.2 eV, 712.1 eV, and 713.2 eV. Note that the attenuation length of the photoelectron is around 10 nm [40] therefore, partial information is obtained from the surface containing an enormous amount of corrosion product. However, it provides essential evidence in determining the oxidized species of elements buried in the corrosion product.

Grazing incidence X-ray diffraction (GIXRD) was performed on 14-days and 1-year immersed specimens, as shown in Fig. 9a, to extract the information from a large volume of corrosion product due to its substantial penetration depth in microns. The diffraction pattern exhibited that the corrosion product was build-up mostly of $Al(OH)_3$ with the presence of Al_2O_3, a slight amount of Fe_2O_3, and hydroxides such as FeO(OH) and $Cu(OH)_2$. The Al peaks were observed in both

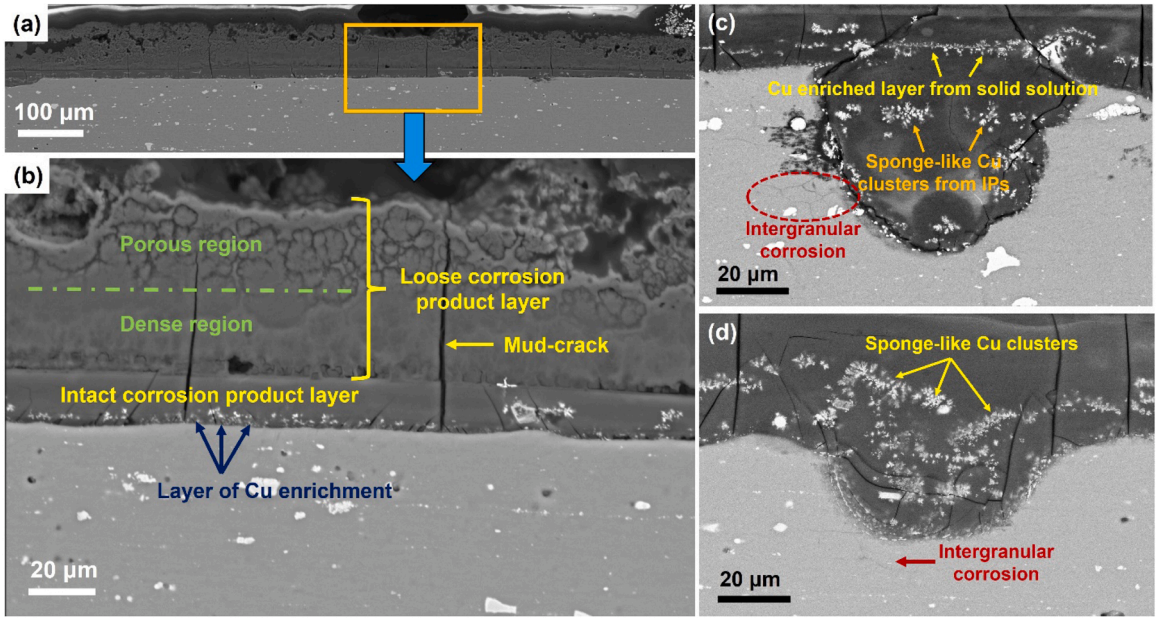

Fig. 6. (a) Low magnification cross-sectional view of AA2024-T3 after 1 year immersion in 0.1 M NaCl, and (b) magnified image showing the morphological distribution within corrosion product and Cu-enrichment at the interface, (c, d) show large pit formation exhibiting Cu clusters from IPs and Cu enrichment at hydroxide/metal interface coming from solid solution. The pit vicinity is also showing intergranular corrosion.

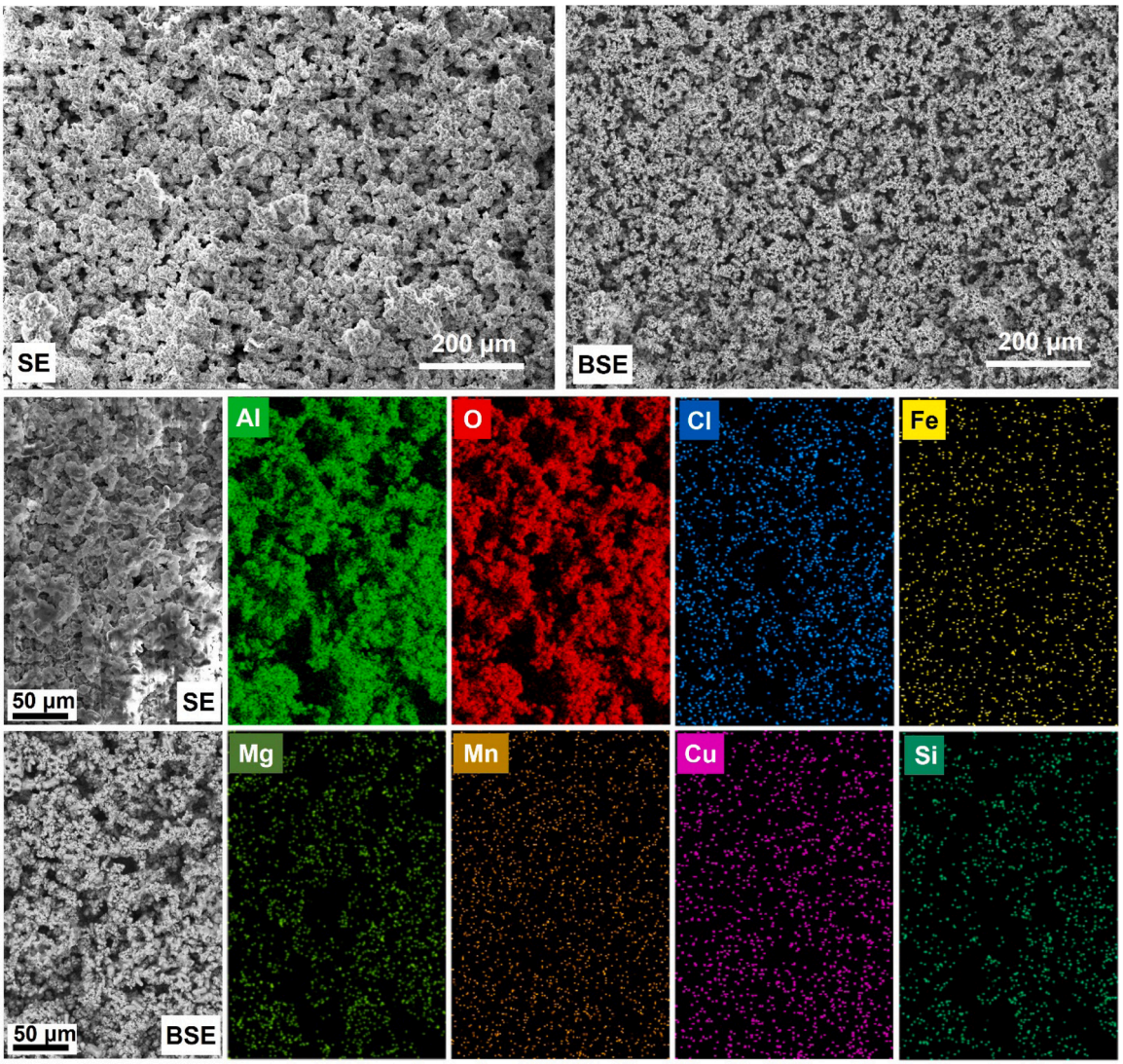

Fig. 7. SEM images of AA2024-T3 top view showing the corrosion product after 1 year immersion in 0.1 M NaCl along with the EDS mapping exhibiting the elemental distribution.

specimens, and interestingly, the intensities of metallic Al peaks were higher in the 1-year immersed specimen than in the 14-days immersed specimen, although the corrosion product was considerably thick after 1 year, which indicates the presence of unoxidized Al within the corrosion product. The presence of unoxidized Al could happen due to exfoliation corrosion, where the exfoliated grains would be separated from the underlying metal by the corrosion product. Meanwhile, indexing several peaks were challenging as they were overlapping due to many elemental compositions forming oxides in this alloy.

The corrosion product is mainly comprised of a high amount of hydroxide and thereafter oxide, as confirmed by XPS and GIXRD. The plot of corrosion product thickness as a function of the immersion period is shown in Fig. 9b. The loose corrosion product tends to grow rapidly in the initial stage, followed by a gradual drop in the growth rate with the immersion period. Meanwhile, the intact layer does not seem to increase significantly compared to the loose corrosion product, and its growth rate appears to increase slightly with the immersion period.

4. Discussions

The decrease in the growth of loose corrosion product with time indicates that the adequate electrolyte is not able to access the metallic alloy surface easily and is obstructed by the intact corrosion product. The corrosion product is reported to act as a hindrance and block the penetration of the aggressive ions up to a certain extent [21,41]. The loose corrosion product having a porous structure could potentially allow the penetration of electrolyte while the intact corrosion product could control the diffusion of metal cations and aggressive anions such as O^{2-} and Cl^{-} ions through ionic transportation. Also, with long-term exposure to an aggressive environment, the kinetics and dynamics of anion-cation transportation will tend to depend upon the chemical composition, morphology, and growth of the corrosion product. Besides, IPs acting as cathodic sites would preferentially increase the oxygen reduction and the amount of OH^{-} ions, as confirmed from Fig. 3b, thus locally increasing the rate of dissolution and pH. The IPs tend to become more cathodic with the increase in the pH of the environment [42] and corrosion would accelerate around the cathodic sites.

4.1. Behavior of Al-Cu-Fe-Mn particle

The cathodic IPs such as Al-Cu-Fe-Mn does not seem to fall off easily after the formation of corrosion product in large amount around them. Consequently, the extended exposure of cathodic IPs to chloride solution can cause severe damage to the local region as it can accelerate the

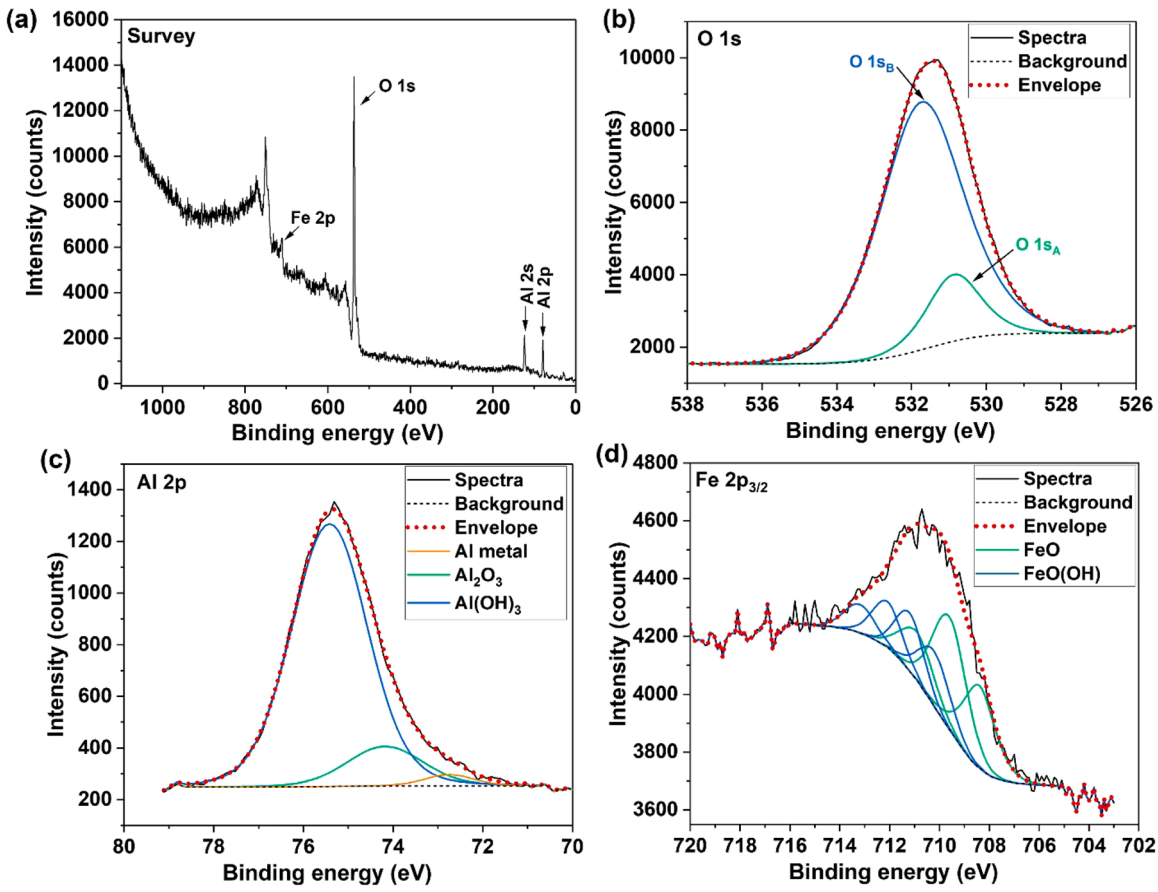

Fig. 8. XPS spectra of AA2024-T3 after 1 year immersion in 0.1 M NaCl showing (a) Survey, (b) O 1s, (c) Al 2p, and (d) Fe $2p_{3/2}$.

Table 2
Binding energies (BE), full-widths at half maximum (FWHM), and intensities (in atomic percent) of the core-level spectra for AA2024-T3 specimen after 1 year immersion in 0.1 M NaCl.

Peak	BE (eV)	FWHM	Intensity (at%)
O $1s_A$	530.87	1.7	9.75
O $1s_B$	531.73	2.6	56.05
Al	72.75	1.3	0.76
Al_2O_3	74.18	2.0	4.13
$Al(OH)_3$	75.42	2.0	27.36
FeO 1	708.40	1.5	0.38
FeO 2	709.60	1.6	0.53
FeO 3	710.90	1.6	0.23
FeO(OH) 1	710.20	1.5	0.24
FeO(OH) 2	711.20	1.34	0.23
FeO(OH) 3	712.10	1.4	0.19
FeO(OH) 4	713.20	1.45	0.12

generated aggressive acidic solution within the pit [43]. As a result, the pit grows. During the growth, it would encounter other nearby IPs, which would further accelerate the pitting phenomena, and gradually, these IPs become part of a large pit (Fig. 6c and 6d).

Moreover, the IPs also undergo dissolution, and Fig. 10 illustrates the schematic diagram of the dealloying of Al-Cu-Fe-Mn particle based on observations and analysis conducted in Fig. 5b. The presence of Cu clusters can be understood by the electrochemical series of metals [44], where the reactivity of elements decreases in the order of Al (active) > Mn > Fe > Cu (noble). Similarly, the order of oxide formation energy decreases in the order of CuO > Fe_2O_3 > MnO > Al_2O_3 having the values of -0.943, -1.707, -1.974, -3.41 eV/atom, respectively [36, 45–47]. The lower the formation energy, the faster the reaction. The low formation energy to form oxides of Al, Mn, and Fe compared to Cu would allow these elements to preferentially react and diffuse early within hydroxide-rich corrosion product, leaving behind Cu remnants in their metallic or oxide form. These Cu remnants could redistribute themselves within its proximity to cause secondary pitting corrosion [5,19]. Literature has also reported that Cu nano-fragments as cuprous (Cu^+) ions or cupric (Cu^{2+}) ions are re-deposited back to the alloy surface preferentially on local cathodes [48]. Consequently, with time, the Cu structure coarsens to reduce its surface energy by dispersing into porous fragments. The electrochemical reactions can be complicated further since the cathodes have a finite lifetime [16]. These Cu fragments would now stop functioning as cathode since it is disconnected from the Al matrix and undergo further oxidation to form complex species with Cu^+ and Cu^{2+}, which was not electrochemically possible when attached to the surface [16]. Such phenomenon evidences the behavior of Cu to stay in clusters for a longer period before it coarsens by forming a sponge-like structure. From Fig. 6a and 6b, the Cu clusters were mainly observed within the intact layer, while there was no trace of the sponge-like or Cu clusters within loose corrosion product, which would be the result of self-dissolution of these Cu clusters at its corrosion potential by ready availability of oxygen and Cl^- ions at top part compared to the sub-level of corrosion product. Thus, the Cu remnants would have eventually dispersed away into the loose corrosion product with time.

4.2. *Intergranular corrosion (IGC) and exfoliation corrosion*

The intergranular attack near the periphery of pits formed after 6 months and 1 year immersion in 0.1 M NaCl exhibited evidence of IGC, while the surface beneath the uniform corrosion did not show any indication of IGC. Meanwhile, the evidence of exfoliation corrosion was confirmed in some regions shown in SEM images and through XRD

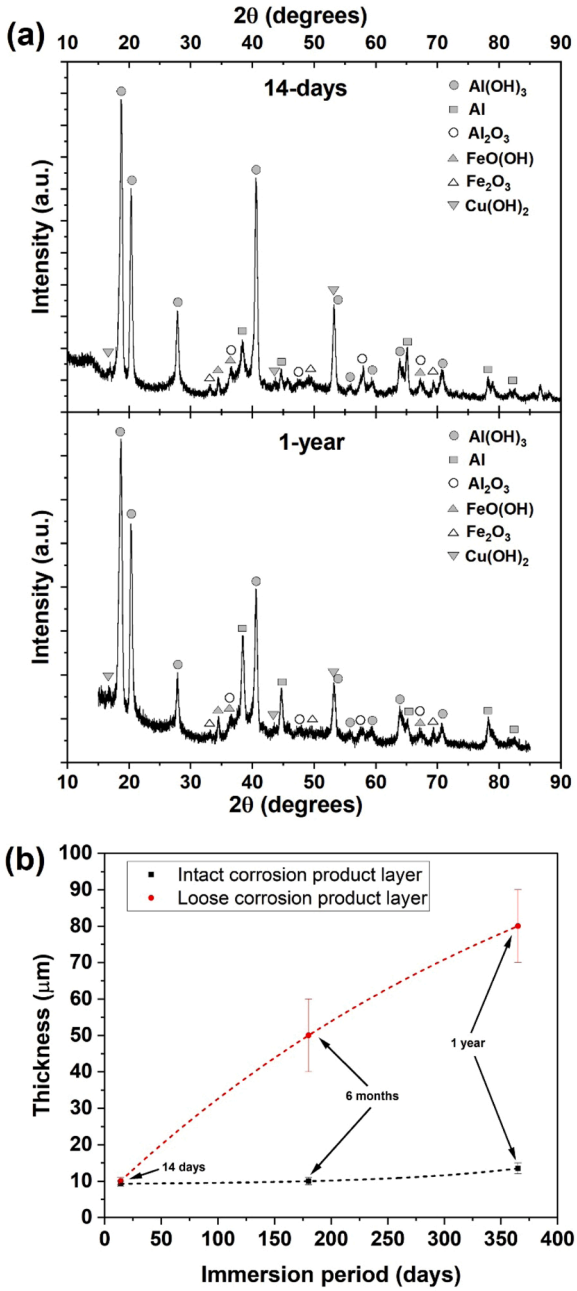

Fig. 9. (a) GIXRD performed on top surface of 14-days and 1-year immersed AA2024-T3 specimens, and (b) plot showing the corrosion product thickness in AA2024-T3 with increase in immersion period in 0.1 M NaCl. The data was plotted based on SEM analysis.

analysis showing the increasing presence of unoxidized Al within the corrosion product. Literature has widely reported the IGC and exfoliation corrosion in AA2024-T3 [35,49,50]. These types of corrosions were severely seen at higher concentrations of NaCl (~1 M). The intensity of exfoliation corrosion was comparably lower in this study, while the events of pitting and uniform corrosion were governing, which could be attributed to a lower concentration of chloride solution.

The main events occurring over the surface and sub-surface are illustrated through the schematic diagram shown in Fig. 11. The initiation of exfoliated grains guides the electrolyte from the surface and provide aggressive anions such as O^{2-} and Cl^{-} ions to promote the oxidation-reduction reaction. As these aggressive anions approach the sub-surface through exfoliated path, hydrolysis of Al^{3+} would occur by forming $Al(OH)_3$ and H^{+} ions, decreasing the pH at that region. The generation of acidic conditions will destabilize the neighboring matrix, and dissolution begins simultaneously from the sub-surface, thereby resulting in severely rapid corrosion activity [21]. The observation showed that the intergranular attack formed a linking path to connect the IPs and was reported by other literature [21,22]. The IPs are in close proximity to each other in the microstructure, which make the network of IPs act as a linking path for exfoliation. The reason for such behavior is not apparent. One of the hypotheses could be the difference in the residual stress between the matrix and IPs, which could channel the exfoliated path towards the IPs.

Most of the time, the surface study does not consider the damage done by sub-surface activity and underestimates the influence of exfoliated regions caused at the sub-surface level. Importantly, a huge amount of corrosion product formed on the surface can control the anion availability and anion-cation transportation. The cross-sectional analysis reported in this work exposes the surface phenomena from a different perspective and rationalizes the entire corrosion phenomena that are sometimes hidden beneath the surface.

5. Conclusions

This study demonstrated the surface and sub-surface corrosion activity of AA2024-T3 by observing the cross-sections of AA2024-T3 after exposure to 0.1 M NaCl for 14 days, 6 months, and 1 year. The cross-sectional analysis shown here allows investigation of the large area and reveals the tens of microns thick corrosion product, size and shape of pits, progressive dissolution of IPs, and exfoliated regions. Following are the conclusions drawn from this work.

1) The corrosion product generated on the surface consisted of mainly two layers – an intact corrosion product layer that is compact and tightly embedded with the surface, and a loose corrosion product layer that has an irregularly porous structure. The porous layer would potentially allow the electrolyte to penetrate, while the compact layer would control the penetration through ionic transportation. Both the layers showed growth over the immersion period, where the loose corrosion product layer exhibited significant growth comparatively.
2) The region within the corrosion product and large pits displayed local sponge-like and solid Cu clusters generated from IPs, while the uniform layer of Cu enrichment was observed across the corrosion product/metal interface potentially generated from the decomposition of solid solution and nano-sized precipitates.
3) The progressive dissolution of the Al-Cu-Fe-Mn particle demonstrated the numerous Cu fragments detaching from the particle while the elements: Al, Mn, and Fe were preferentially oxidized and diffused within the corrosion product. These Cu fragments could redistribute to the alloy surface and promote secondary pitting corrosion. Eventually, with time, once these fragments of Cu clusters are no longer attached to the matrix, they would cease to act as cathodes and would further oxidize to form a sponge-like structure and gradually disperse away within the corrosion product.
4) The AA2024-T3 alloy showed different types of corrosion, such as uniform, pitting, intergranular, and exfoliation. The exfoliation corrosion was observed to propagate through two paths: grain boundaries (IGC) and IPs. The network of exfoliated path can guide the electrolyte by providing aggressive anions to initiate the oxidation-reduction reaction, which can promote dissolution at the sub-surface region, causing severely rapid deterioration.

CRediT authorship contribution statement

J. Christudasjustus: Conceptualization, Methodology, Investigation, Formal analysis, Data curation, Writing – original draft, Writing – review & editing. **V.B. Vukkum**: Methodology, Investigation, Formal analysis, Writing – review & editing. **R.K. Gupta:** Conceptualization,

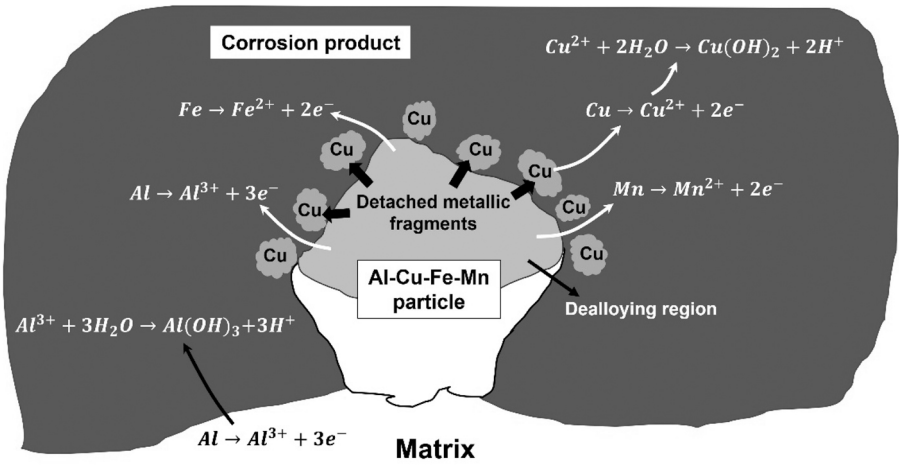

Fig. 10. Schematic diagram showing dissolution mechanism of Al-Cu-Fe-Mn particle in AA2024-T3.

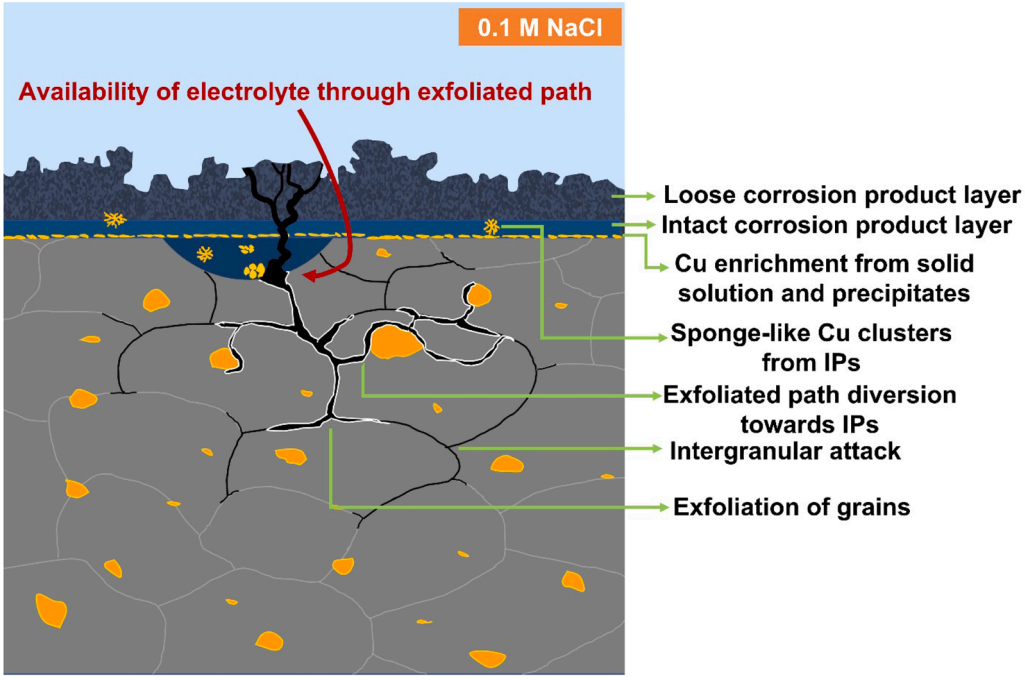

Fig. 11. Schematic diagram representing the surface/sub-surface features and exfoliation corrosion along intergranular and IPs in AA2024-T3.

Methodology, Writing – review & editing, Supervision, Project administration, Funding acquisition.

Declaration of Competing Interest

The authors declare that they have no known competing financial interests or personal relationships that could have appeared to influence the work reported in this paper.

Data availability

Data will be made available on request.

Acknowledgments

The authors would like to acknowledge the financial support received from the National Science Foundation (Nos. NSF-CMMI 1760204 and NSF-CMMI 2131440) under the direction of Dr. Alexis Lewis. This work was performed in part at the Analytical Instrumentation Facility (AIF) at North Carolina State University, which is supported by the State of North Carolina and the National Science Foundation (award number ECCS-2025064). The AIF is a member of the North Carolina Research Triangle Nanotechnology Network (RTNN), a site in the National Nanotechnology Coordinated Infrastructure (NNCI).

References

[1] A.E. Hughes, R. Parvizi, M. Forsyth, Microstructure and corrosion of AA2024, Corros. Rev. 33 (2015) 1–30, https://doi.org/10.1515/corrrev-2014-0039.
[2] I.J. Polmear, Light Alloys, Butterworth-Heinemann, 2005, https://doi.org/10.1016/B978-0-7506-6371-7.X5000-2.
[3] J.G. Kaufman, Introduction to Aluminium Alloys and Tempers, ASM International, 2000.
[4] R.K. Gupta, N.L. Sukiman, M.K. Cavanaugh, B.R.W. Hinton, C.R. Hutchinson, N. Birbilis, Metastable pitting characteristics of aluminium alloys measured using current transients during potentiostatic polarisation, Electrochim. Acta 66 (2012) 245–254, https://doi.org/10.1016/J.ELECTACTA.2012.01.090.

[5] R.G. Buchheit, R.P. Grant, P.F. Hiava, B. Mckenzie, G. Zender, Local dissolution phenomena associated with S phase (Al2CuMg) particles in aluminum alloy 2024-T3, J. Electrochem. Soc. 144 (1997) 2621–2628.

[6] M.A. Jakab, D.A. Little, J.R. Scully, Experimental and modeling studies of the oxygen reduction reaction on AA2024-T3, J. Electrochem. Soc. 152 (2005) B311, https://doi.org/10.1149/1.1949047/XML.

[7] G.O. Ilevbare, O. Schneider, R.G. Kelly, J.R. Scully, In situ confocal laser scanning microscopy of AA 2024-T3 corrosion metrology: I. Localized corrosion of particles, J. Electrochem. Soc. 151 (2004) B453–B464, https://doi.org/10.1149/1.1764780.

[8] A. Boag, A.E. Hughes, N.C. Wilson, A. Torpy, C.M. MacRae, A.M. Glenn, T. H. Muster, How complex is the microstructure of AA2024-T3, Corros. Sci. 51 (2009) 1565–1568, https://doi.org/10.1016/j.corsci.2009.05.001.

[9] W. Zhang, G.S. Frankel, Transitions between pitting and intergranular corrosion in AA2024, Electrochim. Acta 48 (2003) 1193–1210, https://doi.org/10.1016/S0013-4686(02)00828-9.

[10] J. Wang, B. Zhang, Y.T. Zhou, X.L. Ma, Multiple twins of a decagonal approximant embedded in S-Al2CuMg phase resulting in pitting initiation of a 2024Al alloy, Acta Mater. 82 (2015) 22–31, https://doi.org/10.1016/J.ACTAMAT.2014.09.001.

[11] J.O. Park, C.H. Paik, Y.H. Huang, R.C. Alkire, Influence of Fe-rich intermetallic inclusions on pit initiation on aluminum alloys in aerated NaCl, J. Electrochem. Soc. 146 (1999) 517–523.

[12] L. Yin, Y. Jin, C. Leygraf, N. Birbilis, J. Pan, Numerical simulation of micro-galvanic corrosion in Al alloys: effect of geometric factors, J. Electrochem. Soc. 164 (2017) C75–C84, https://doi.org/10.1149/2.1221702JES/XML.

[13] M.B. Vukmirovic, N. Dimitrov, K. Sieradzki, Dealloying and corrosion of Al alloy 2024-T3, J. Electrochem. Soc. 149 (2002) B428–B439, https://doi.org/10.1149/1.1498258.

[14] A. Kosari, F. Tichelaar, P. Visser, H. Zandbergen, H. Terryn, J.M.C. Mol, Dealloying-driven local corrosion by intermetallic constituent particles and dispersoids in aerospace aluminium alloys, Corros. Sci. 177 (2020), 108947, https://doi.org/10.1016/J.CORSCI.2020.108947.

[15] P. Leblanc, G.S. Frankel, A study of corrosion and pitting initiation of AA2024-T3 using atomic force microscopy, J. Electrochem. Soc. 149 (2002) B239–B247, https://doi.org/10.1149/1.1471546/XML.

[16] R.G. Buchheit, M.A. Martinez, L.P. Montes, Evidence for Cu ion formation by dissolution and dealloying the Al2CuMg intermetallic compound in rotating ring-disk collection experiments, J. Electrochem. Soc. 147 (2000) 119–124.

[17] A.E. Hughes, A. Boag, A.M. Glenn, D. McCulloch, T.H. Muster, C. Ryan, C. Luo, X. Zhou, G.E. Thompson, Corrosion of AA2024-T3 part II: Co-operative corrosion, Corros. Sci. 53 (2011) 27–39, https://doi.org/10.1016/j.corsci.2010.09.030.

[18] D. Zhu, W.J. van Ooij, Corrosion protection of AA 2024-T3 by bis-[3-(triethoxysilyl)propyl]tetrasulfide in neutral sodium chloride solution. Part 1: corrosion of AA 2024-T3, Corros. Sci. 45 (2003) 2163–2175, https://doi.org/10.1016/S0010-938X(03)00060-X.

[19] N. Dimotrov, J.A. Mann, K. Sieradzki, Copper redistribution during corrosion of aluminum alloys, J. Electrochem. Soc. 146 (1999) 98–102.

[20] X. Zhang, T. Hashimoto, J. Lindsay, X. Zhou, Investigation of the de-alloying behaviour of θ-phase (Al2Cu) in AA2024-T351 aluminium alloy, Corros. Sci. 108 (2016) 85–93, https://doi.org/10.1016/J.CORSCI.2016.03.003.

[21] P.C. King, I.S. Cole, P.A. Corrigan, A.E. Hughes, T.H. Muster, FIB/SEM study of AA2024 corrosion under a seawater drop: part I, Corros. Sci. 53 (2011) 1086–1096, https://doi.org/10.1016/j.corsci.2010.12.004.

[22] P.C. King, I.S. Cole, P.A. Corrigan, A.E. Hughes, T.H. Muster, S. Thomas, FIB/SEM study of AA2024 corrosion under a seawater drop, part II, Corros. Sci. 55 (2012) 116–125, https://doi.org/10.1016/j.corsci.2011.10.012.

[23] I.W. Huang, B.L. Hurley, F. Yang, R.G. Buchheit, Dependence on temperature, pH, and Cl- in the uniform corrosion of aluminum alloys 2024-T3, 6061-T6, and 7075-T6, Electrochim. Acta 199 (2016) 242–253, https://doi.org/10.1016/J.ELECTACTA.2016.03.125.

[24] I-Wen Huang, Uniform Corrosion and General Dissolution of Aluminum Alloys 2024-T3, 6061-T6, and 7075-T6, The Ohio State University, 2016. ⟨http://rave.ohiolink.edu/etdc/view?acc_num=osu1469105977⟩, (Accessed 30 March 2022).

[25] T. Tsuda, Y. Ikeda, T. Arimura, A. Imanishi, S. Kuwabata, C. Hussey, G. Stafford, Al-W alloy deposition from lewis acidic room-temperature chloroaluminate ionic liquid, ECS Trans. 50 (2012) 239–250, https://doi.org/10.1149/ma2012-02/53/3635.

[26] G.S. Frankel, R.C. Newman, C.v. Jahnes, M.A. Russak, On the pitting resistance of sputter-deposited aluminum alloys, J. Electrochem. Soc. 140 (1993) 2192–2197, https://doi.org/10.1149/1.2220794/XML.

[27] F. Ozdemir, C.S. Witharamage, J. Christudasjustus, A.A. Darwish, H. Okuyucu, R. K. Gupta, Corrosion behavior of a bulk nanocrystalline Al-Fe alloy, Corros. Sci. 209 (2022), 110727, https://doi.org/10.1016/J.CORSCI.2022.110727.

[28] C.S. Witharamage, J. Christudasjustus, J. Smith, W. Gao, R.K. Gupta, Corrosion behavior of an in situ consolidated nanocrystalline Al-V alloy, npj Mater. Degrad. 6 (2022) 1–9, https://doi.org/10.1038/s41529-022-00225-5.

[29] J. Esquivel, R.K. Gupta, Review—corrosion-resistant metastable Al alloys: an overview of corrosion mechanisms, J. Electrochem. Soc. 167 (2020), 081504, https://doi.org/10.1149/1945-7111/AB8A97.

[30] R.K. Gupta, D. Fabijanic, R. Zhang, N. Birbilis, Corrosion behaviour and hardness of in situ consolidated nanostructured Al and Al-Cr alloys produced via high-energy ball milling, Corros. Sci. 98 (2015) 643–650, https://doi.org/10.1016/j.corsci.2015.06.011.

[31] J. Christudasjustus, M.R. Felde, C.S. Witharamage, J. Esquivel, A.A. Darwish, C. Winkler, R.K. Gupta, Age-hardening behavior, corrosion mechanisms, and passive film structure of nanocrystalline Al-V supersaturated solid solution, J. Mater. Sci. Technol. 135 (2023) 1–12, https://doi.org/10.1016/J.JMST.2022.06.044.

[32] I.-W. Huang, R.G. Buchheit, Uniform corrosion dependence on temperature and pH of aluminum alloys 2024-T3, J. Electrochem. Soc. 66 (2015) 97–107, https://doi.org/10.1149/06617.0097ecst.

[33] J.H. Scofield, Hartree-Slater subshell photoionization cross-sections at 1254 and 1487 eV, J. Electron Spectrosc. Relat. Phenom. 8 (1976) 129–137, https://doi.org/10.1016/0368-2048(76)80015-1.

[34] H. Habazaki, K. Shimizu, P. Skeldon, G.E. Thompson, G.C. Wood, X. Zhou, Effects of alloying elements in anodizing of aluminium, Trans. Inst. Met. Finish. 75 (1997) 18–23, https://doi.org/10.1080/00202967.1997.11871137.

[35] X. Liu, G.S. Frankel, B. Zoofan, S.I. Rokhlin, Effect of applied tensile stress on intergranular corrosion of AA2024-T3, Corros. Sci. 46 (2004) 405–425, https://doi.org/10.1016/S0010-938X(03)00149-5.

[36] The Materials Project, Materials Data for Al2O3 (mp-1143) from Database Version v2021.11.10, Materials Project, 2020. ⟨https://doi.org/10.17188/1187823⟩.

[37] The Materials Project, Materials Data on Al(HO)3 by Materials Project, Materials Project, 2020. ⟨https://doi.org/10.17188/1201766⟩.

[38] A.P. Grosvenor, B.A. Kobe, M.C. Biesinger, N.S. McIntyre, Investigation of multiplet splitting of Fe 2p XPS spectra and bonding in iron compounds, Surf. Interface Anal. 36 (2004) 1564–1574, https://doi.org/10.1002/SIA.1984.

[39] M.C. Biesinger, B.P. Payne, A.P. Grosvenor, L.W.M. Lau, A.R. Gerson, R.S.C. Smart, Resolving surface chemical states in XPS analysis of first row transition metals, oxides and hydroxides: Cr, Mn, Fe, Co and Ni, Appl. Surf. Sci. 257 (2011) 2717–2730, https://doi.org/10.1016/j.apsusc.2010.10.051.

[40] B. Díaz, E. Härkönen, J. Światowska, V. Maurice, A. Seyeux, P. Marcus, M. Ritala, Low-temperature atomic layer deposition of Al2O3 thin coatings for corrosion protection of steel: Surface and electrochemical analysis, Corros. Sci. 53 (2011) 2168–2175, https://doi.org/10.1016/j.corsci.2011.02.036.

[41] J.A. Moreto, C.E.B. Marino, W.W. Bose Filho, L.A. Rocha, J.C.S. Fernandes, SVET, SKP and EIS study of the corrosion behaviour of high strength Al and Al-Li alloys used in aircraft fabrication, Corros. Sci. 84 (2014) 30–41, https://doi.org/10.1016/j.corsci.2014.03.001.

[42] N. Birbilis, R.G. Buchheit, Investigation and discussion of characteristics for intermetallic phases common to aluminum alloys as a function of solution pH, J. Electrochem. Soc. 155 (2008) C117–C126, https://doi.org/10.1149/1.2829897.

[43] G.S. Frankel, Pitting corrosion of metals: a review of the critical factors, J. Electrochem. Soc. 145 (1998) 2186–2198, https://doi.org/10.1149/1.1838615/XML.

[44] E. Mccafferty. Introduction to Corrosion Science, 2009, https://doi.org/10.1007/b97510.

[45] The Materials Project, Materials Data for CuO (mp-704645) from Database Version v2021.11.10, Materials Project, 2021.

[46] The Materials Project, Materials Data for Fe2O3 (mp-19770) from Database Version v2021.11.10, Materials Project, 2021. ⟨https://materialsproject.org/materials/mp-19770/⟩.

[47] The Materials Project, Materials Data for MnO (mp-19006) from Database Version v2021.11.10, Materials Project, 2020.

[48] C. Luo. Role of Microstructure on Corrosion Control of AA2024-T3 Aluminium Alloy, The University of Manchester, 2011.

[49] W. Zhang, G.S. Frankel, Transitions between pitting and intergranular corrosion in AA2024, Electrochim. Acta 48 (2003) 1193–1210, https://doi.org/10.1016/S0013-4686(02)00828-9.

[50] N.D. Alexopoulos, On the corrosion-induced mechanical degradation for different artificial aging conditions of 2024 aluminum alloy, Mater. Sci. Eng. A 520 (2009) 40–48, https://doi.org/10.1016/J.MSEA.2009.05.023.